Crystal and magnetic structural study of the $La_{1-x}Ca_xMnO_3$ compound $\left(x=\frac{3}{4}\right)$

M. Pissas,[1] I. Margiolaki,[2] K. Prassides,[3] and E. Suard[4]
[1]*Institute of Materials Science, National Center for Scientific Research Demokritos, 153 10 Ag. Paraskevi, Athens, Greece*
[2]*European Synchrotron Radiation Facility, 38043 Grenoble Cedex 9, France*
[3]*Department of Chemistry, University of Durham, South Road, Durham DH1 3LE, United Kingdom*
[4]*Institut Laue Langevin, Boîte Postal 156, 38042 Grenoble, France*
(Received 31 March 2005; revised manuscript received 24 June 2005; published 15 August 2005)

We studied the crystal and magnetic structure of the $La_{1/4}Ca_{3/4}MnO_3$ compound using ultrahigh resolution synchrotron x-ray and neutron-diffraction techniques. The experimental results revealed that the particular compound undergoes a structural transition at $T_{CO}=220$ K. This transition results in an increase of the orthorhombic splitting and the appearance of superlattice diffraction peaks, which can be indexed assuming a supercell $4a$ (a is the unit cell parameter for $T>T_{CO}$). This transition is reminiscent of those observed for the $x=1/2$ and $x=2/3$ stoichiometries where superstructures with $2a$ and $3a$, respectively, have been observed. At $T_N=160$ K the neutron-diffraction patterns exhibit additional diffraction peaks, corresponding to antiferromagnetic long-range order with propagation vectors $\mathbf{k}=\left[\frac{1}{4},0,\frac{1}{2}\right]$ and $\mathbf{k}=\left[\frac{1}{2},0,\frac{1}{2}\right]$. In addition to the structural transition at T_{CO} the synchrotron high resolution x-ray diffraction patterns revealed a three phase coexistence.

DOI: 10.1103/PhysRevB.72.064426 PACS number(s): 75.47.Lx, 61.10.Nz, 61.12.Ld, 81.30.−t

I. INTRODUCTION

Rare-earth manganite perovskites exhibit complex phase diagrams associated with the interplay of charge, spin, orbital, and lattice degrees of freedom.[1] An important open issue in understanding the physics of manganites is the phase transition to charge (CO) and orbital (OO) ordered phases which has been suggested to occur upon cooling. The $La_{1-x}Ca_xMnO_3$ $(0<x<1)$ series has been studied in considerable detail and was found to display a rich phase diagram. In particular, for $0.23<x<0.45$, the compounds are metallic ferromagnets. For all other calcium concentrations x, the ground state is insulating. For compositions with $x>0.5$, the insulating behavior has been attributed to the occurrence of charge ordering below a critical temperature T_{CO}. In particular, for $x=\frac{1}{2}$ and $x=\frac{2}{3}$ and $T<T_{CO}$, superstructures with periodicities of $2a$ and $3a$, respectively (where a refers to the lattice dimensions along the a axis of the high-temperature orthorhombic unit cell, space group *Pnma*) have been observed. Crystal and magnetic structural refinements[2,3] favor a model of real space charge and orbital ordering of Mn charges and Mn-e_g orbitals. Within this charge ordered model, the crystal structure consists of planes, parallel to bc, of Mn ions with the same charge (3+ or 4+). The stacking of these planes is commensurate with $n/(n+1)$ $(n=1,2)$, where n is the ratio of the alkaline earth content $1-x$ over the lanthanide doping level x.

The stability of the CO state may be related to the commensurability of the hole concentration with the lattice periodicity and is enhanced at nominal hole concentrations of $\frac{1}{2}$, $\frac{2}{3}$, and $\frac{3}{4}$. For the noncommensurate (arbitrary) electron concentrations, the experimental situation is not unique. Contrast seen in electron diffraction microscopy images (if for the moment we ignore the Jahn-Teller-stripes–Wigner crystal debate) has been interpreted in terms of proper mixtures of the two adjacent distinct commensurate configurations according to the lever rule. For example, the $x=\frac{5}{8}$ composition, which straddles the charge-ordered $x=\frac{1}{2}$ and $\frac{2}{3}$ systems, has been proposed[4] to exhibit a fine mixture of 25% $2a$ and 75% $3a$ charge ordered states. In this model, the term "fine mixture" does not imply that the sample is macroscopically phase separated, but rather that it consists of incoherent stacking-fault defects in an otherwise perfect $3a$ configuration.[4] The probability of observing the minority $2a$ superstructure is given by the application of the lever rule. This model has been used to interpret neutron diffraction[5] and Mössbauer data[6] for compounds with arbitrary carrier concentrations. In these cases, the observed magnetic diffraction peaks correspond to the two adjacent distinct commensurate configurations.[5] Recently, Loudon *et al.*[7] have criticized the idealized Mn^{3+} and Mn^{4+} charge stripe model, based on their observations of electron-diffraction patterns collected at 90 K with a convergent beam of 36 Å diameter. The observed modulations in the $0.5\leqslant x\leqslant 0.71$ stoichiometry regime could not be described as a fine mixture of integer period sub-units delineated by discommensurations. Instead their results are in favor of a uniform periodicity at any doping level with $x\geqslant 0.5$, ruling out the existence of just two types of lattice planes occupied exclusively by Mn^{4+} and Mn^{3+} ions. We also emphasize that several recent studies[8–11] favor neither an integer (Mn^{3+}/Mn^{4+}) charge Wigner crystal model nor a paired striped model but instead one with non-integral charges (e.g., $Mn^{3+\delta}/Mn^{4-\delta}$).

For $0.8\leqslant x\leqslant 0.85$, neutron-diffraction data do not reveal the presence of charge-ordered structures. Instead, the so-called C structure is observed.[12] Therefore, the phase boundary near the onset of the C structure $\left(\frac{2}{3}<x<\frac{4}{5}\right)$ is also intriguing as it involves the change of the ground state from CO to type C, where charge ordering is absent. In addition, in order to obtain additional insight into the applicability of the $n/(n+1)$, $n=1,2,3$ rule, it is important to determine the crystal structure of the $x=\frac{3}{4}$ compound, which is not currently available. Electron-diffraction data[4,13] have revealed superstructure peaks with modulation vector $\mathbf{k}=\left[\frac{1}{4},0,0\right]$, a

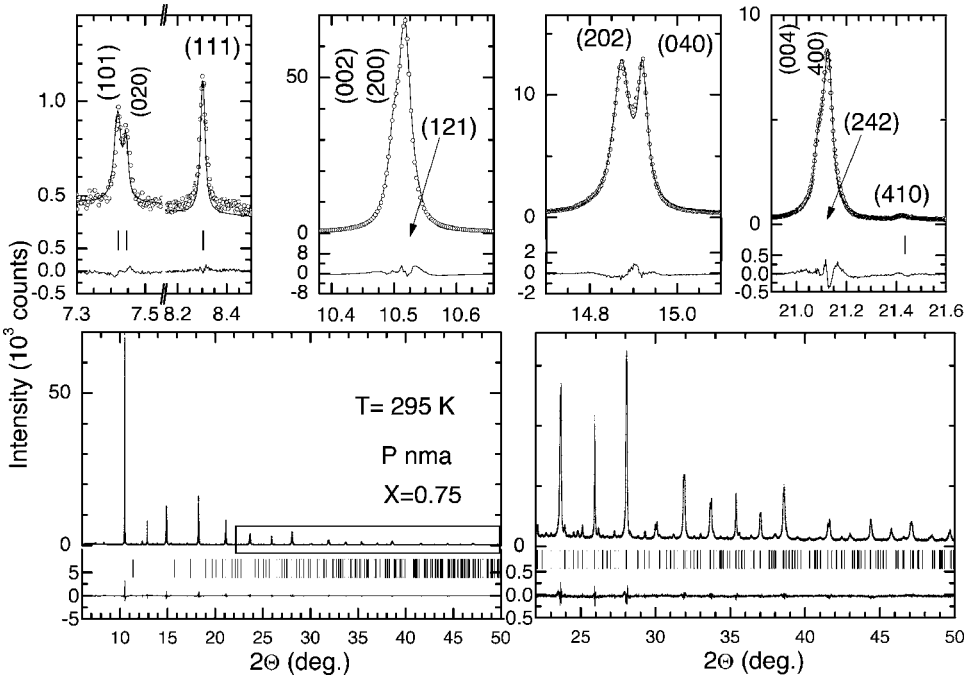

FIG. 1. Selected regions of the observed (○) and calculated (solid line) synchrotron x-ray powder ($T=295$ K, $\lambda=0.48994$ Å) diffraction profiles of $La_{0.25}Ca_{0.75}MnO_3$ with the characteristic peak splittings, compatible with the *Pnma* space group evident. The lower solid lines show the difference profiles and the tick marks show the reflection positions. In the lower panels, the Rietveld plot in the full angular range 5°–50° and its expansion for Bragg angles larger than 22° are also shown.

fact that may imply that for this concentration, a charge ordered structure, related to those for $x=\frac{1}{2}$ and $x=\frac{2}{3}$, also forms.

In this article, we present a crystallographic study using the high-resolution synchrotron x-ray-diffraction technique for a carefully prepared $La_{1-x}Ca_xMnO_3$ sample with $x=\frac{3}{4}$. In addition to the experimental demonstration of the presence of a $4a$ superstructure modulation of the crystal structure for this particular carrier concentration, our data also reveal a mesoscopic (macroscopic) coexistence of different phases, which is not the result of a preexisting heterogeneity or martensitic transformation of the material. This complicated "picture" may imply that the physics of manganite perovskites is more complex than a simple charge-ordered model.

II. EXPERIMENTAL DETAILS

The $La_{1/4}Ca_{3/4}MnO_3$ sample was prepared by thoroughly mixing high-purity stoichiometric amounts of $CaCO_3$, La_2O_3, and MnO_2. The mixed powders were reacted in air up to 1400 °C for several days with intermediate grindings. In the final step, the sample was slowly cooled to 25 °C. High-resolution synchrotron x-ray powder diffraction patterns (SXRPD) were collected with the multi-detector powder diffractometer on the ID31 beamline at the ESRF (Grenoble, France) in Debye-Scherrer (transmission) configuration. Powder samples were sealed in thin-wall borosilicate glass capillaries ($d=0.5$ mm), inserted in a continuous-flow cryostat and rotated during data collection. Data were collected at selected temperatures between 5 and 300 K both on cooling and heating at various wavelengths, λ near 0.5 Å. The neutron-powder-diffraction (NPD) experiments were undertaken with the high-resolution diffractometer D2b ($\lambda=1.595$ Å and 2.44 Å) at the Institute Laue Langevin (ILL), Grenoble, France. The sample, 5 g, was loaded in a cylindrical vanadium can (diameter=5 mm) and placed in a standard ILL "orange" liquid helium cryostat. The instrument was operated in both its high-resolution (10′ horizontal primary divergence, 1 cm horizontal monochromator aperture) and high-intensity modes and the data were collected in the angular range $2\theta=0°-164.5°$ in steps of 0.05°. The raw data were merged, whilst applying angular and efficiency (vanadium) detector calibrations, using standard ILL programs. dc magnetization measurements were performed with a superconducting quantum interference device (SQUID) magnetometer (Quantum Design MPMS5). The SXRPD and NPD datasets were refined using the Rietveld method with the FULLPROF and GSAS suites of programs.[14,15]

III. RESULTS

A. Crystal structure

Figure 1 shows selected regions of the high-resolution synchrotron x-ray powder-diffraction pattern of $La_{0.25}Ca_{0.75}MnO_3$ at 295 K. The diffraction profile can be refined successfully with a single phase model in the orthorhombic space group *Pnma*, which describes all the phases of the $La_{1-x}Ca_xMnO_3$ ($x=0-1$) series above the Jahn-Teller and charge ordering temperatures. First, we refined the scale factors, background coefficients, unit cell parameters, zero-shift errors, and peak profile coefficients. As peak profile function, we selected a pseudo-Voigt convoluted with the Finger-Cox-Jephcoat function[16] in order to take into account axial divergence. In the early refinement cycles, we ascertained that the diffraction peaks are characterized by selective peak broadening. This effect is clearly evident in Fig. 1 when one inspects the (202)/(040) doublet. If these peaks were of the same full width at half maximum (FWHM), a height ratio proportional to the theoretically calculated intensity ratio, ≈2:1 would be expected. Contrary to this, they

display nearly the same height, implying a larger FWHM for the (202) reflection. In addition, the Gaussian contribution to the peak shape is very small, $W<10^{-4}$ deg.^{2} with negligible Lorentzian Scherrer broadening, $Y<10^{-4}$ deg. The peak shape appears to be dominated by the Lorentzian contribution, $X\approx 0.223$ deg. due to strain effects. Such type of broadening could be better taken into account by employing the formalism developed by Stephens[17] that yielded much better fits of the peak shapes. It is tempting to associate the observed selective peak broadening with the remarkable softening of the shear modulus observed on approaching the charge ordering temperature T_{CO} (see below) from above.[18] As the shear modulus reaches its minimum value, the lattice becomes unstable to strains and the crystal structure changes to a more distorted, lower symmetry phase. Finally, we performed a combined Rietveld refinement of the SXRPD and NPD profiles, which proceeded smoothly and resulted in very good quality-of-fit factors. The final results are summarized in Table I.

Figure 2 shows selected regions of the SXRPD profile of $La_{0.25}Ca_{0.75}MnO_3$ at 5 K. Exploratory refinements with the orthorhombic structural model used successfully at 295 K immediately reveal the presence of more than one phase. After subtracting the majority phase whose diffraction profile resembles that at 295 K, the difference pattern is very similar to that exhibited by $La_{1-x}Ca_xMnO_3$ at a doping level of $x=0.8$ below $T_{CO}\sim 180$ K. The structural properties of this phase have been analyzed in detail in Ref. 12 and for $T<T_{CO}$, it adopts the so-called C structure, where only orbital ordering without any accompanying charge ordering is present. In addition, this transition is accompanied by a monoclinic distortion ($\beta\approx 91.6°$, space group $P2_1/m$), allowing the facile identification of this phase. A two-phase structural model was therefore employed in the Rietveld refinement of the SXRPD data with satisfactory results (agreement factor $R_{WP}\sim 10\%$). However, careful inspection of the profile near the background level still revealed several weak peaks not accounted for by the two-phase structural model. These peaks can be indexed using fractional Miller indices or equivalently a modulation vector $\mathbf{k}_s=[\delta,0,0]$ with $\delta=\frac{1}{4}$. The strongest superlattice peaks appear as satellites of intense primitive perovskite reflections with in-phase La and Mn contributions and nonzero l Miller indices $[(\frac{3}{4},2,\pm 1)$, $(\frac{5}{4},2,\pm 1)$, $(\frac{7}{4},4,\pm 2)$, $(\frac{9}{4},4,\pm 2)$, $(\frac{11}{4},1,\pm 1)$,$(\frac{3}{4},2,\pm 3)$,$(\frac{5}{4},2,\pm 3)$,$(\frac{5}{4},0,\pm 6)$,$(\frac{7}{4},4,\pm 2)]$. We note that similar satellite peaks but with a components of the structural modulation vector equal to $\frac{1}{2}$ and $\frac{1}{3}$ were observed in $La_{1-x}Ca_xMnO_3$ with $x=\frac{1}{2}$ and $x=\frac{2}{3}$, respectively,[2,3] and provided the diffraction signatures of the charge and orbitally ordered $2a$ and $3a$ superstructures. Therefore these data provide at this stage strong evidence that the majority phase of the $x=\frac{3}{4}$ composition at 5 K corresponds to an analogous CO and OO $4a$ superstructure. Moreover such an observation favors an identical mechanism being responsible for the formation of the superstructures in all three compositions.

Following the successful indexing of the weak superlattice diffraction peaks, careful inspection of the difference profile, $(Y_{obs}-Y_{calc})$ further revealed the presence of additional intensity unaccounted by the two-phase model. Attempts to attribute this to impurity phases were not successful. However, one attractive possibility to consider is that the high-temperature single phase material did not transform completely to the $4a$-superstructure on cooling, but part of it dissociated into two components, namely into the C and $3a$ structures. Indeed, after incorporating the $3a$ structure as a third phase in the Rietveld refinements by using the structural model from Ref. 3, the agreement factors further improved ($\Delta R_{WP}\sim 2.0\%$). Ignoring for the moment the presence of the superlattice Bragg peaks and using an average structural model for the $4a$ superstructure, we refined the SXRPD data at $T=5$ K in order to estimate both the weight fraction of the three phases present and to derive reliable structural parameters for the average $4a$ structure. The weight fractions of the three phases refined to 60(1), 23(1), and 17(2) % for the $4a$, C, and $3a$ structures, respectively. The three-phase decomposition of the SXRPD profile at 5 K in the region of the (202)/(040) doublet is shown in panel (b) of Fig. 2.

Having identified all phases present and the average structure of the majority phase, we are therefore in a position to deal with the modulated $4a$ structure. In order to analyze quantitatively the modulated crystal structure, we employed the simple model developed by Böhm,[19] in which a simple cubic lattice of size a is modulated with an asymmetric rectangular wave of amplitude B and period Ma. D_1a and $(M-D_1)a$ denote the width of the domains and the polarization is assumed to be along the z axis with the modulation wave vector along x. If both M and D_1 are integers, the diffraction intensity of the satellite diffraction peaks with $n=1,2,3,\ldots$, are given by $I(h+n/M,k,l)=|F_0(h,k,l)|^2[2\sin(2\pi lB)\sin(n\pi D_1/M)/M\sin(n\pi/M)]^2$.[19] Here $F_0(h,k,l)$ is the structure factor of the unmodulated unit cell. This transverse modulation model does not predict satellites in the $hk0$ plane in reciprocal space in qualitative agreement with our experimental data and in contrast with its longitudinal counterpart for which satellites in the $hk0$ plane are expected.[20] In addition, the absence of second-order ($n=2$) satellites denotes that the observed modulation is symmetric ($M=4, D_1=2$). Theoretically the first-order satellites are more intense than higher-order ones, a fact also in agreement with the experimental result, although no third order satellites are observed. Furthermore, the most intense satellites observed correspond to main reflections with $l=3$, a fact supporting the assignment of the polarization vector along the c axis.

In applying the above model to our case, we used a unit cell four times larger (along the a axis) than that of the average structure. We also assumed the $P2_1/m$ space group, thereby preserving the reflection planes at $y=\frac{1}{4}$ and $y=\frac{3}{4}$. In this model, there are five Mn sites at $(0,0,\frac{1}{2})$, $(\frac{1}{8},0,0)$, $(\frac{1}{4},0,\frac{1}{2})$, $(\frac{3}{8},0,0)$, and $(\frac{1}{2},0,\frac{1}{2})$ [see Fig. 3(a)]. The Mn and (La, Ca) ions in the $x=0$ and $x=\frac{1}{2}$ planes remain unaffected, while those at $x=\frac{1}{8},\frac{1}{4},\frac{3}{8}$ and at $x=\frac{5}{8},\frac{3}{4},\frac{7}{8}$ shift along the z axis in opposite directions (negative and positive, respectively). This rectangular displacement modulation model can by realized by adopting two additional structural parameters, describing the rigid shift of the Mn^{4+} octahedra and of the neighboring La^{3+} ions, respectively [see Fig. 3(a)]. The

TABLE I. Results of the Rietveld refinement for $La_{1/4}Ca_{3/4}MnO_3$ [$T=295$ K: combined refinement of SXRPD ($\lambda=0.48994$ Å) and NPD ($\lambda=1.594$ Å) data; $T=5$ K: average structure refined from NPD ($\lambda=1.594$ Å) data, superstructure refined from SXRPD ($\lambda=0.50187$ Å) data]. At $T=295$ K, a single phase structural model based on the space group *Pnma* (No. 62) was used. The La, Ca, and apical oxygen (O1) atoms occupy the 4*c*, $(x,\frac{1}{4},z)$ site, Mn the 4*b* $(0,0,\frac{1}{2})$ site and the equatorial oxygen (O2) atom the general 8*d* (x,y,z) site. At $T=5$ K, a three-phase structural model was used, comprising the 4*a* superstructure (majority phase, space group $P2_1/m$) and two minority phases, *C* structure (space group $P2_1/m$) and 3*a* structure (space group *Pnma*). $(x_a^{La},\frac{1}{4},z_a^{La})$, $(x_a^{O1},\frac{1}{4},z_a^{O1})$, and $(x_a^{O2},y_a^{O2},z_a^{O2})$ are the fractional coordinates of the La, O1 and O2 atoms in the average structure model at $T=5$ K. Numbers in parentheses are statistical errors at the last significant digit.

T (K)	295 K	5 K 4*a* superstructure, $\Delta z=-0.015(1)$, $\Delta z_1=-0.018(1)$, $P2_1/m$							
a (Å)	5.35142(6)	21.4732(1)							
b (Å)	7.54682(4)	7.4689(1)							
c (Å)	5.35579(6)	5.3750(1), $\beta=90°$							
La		La1	La2	La3	La4	La5	La6	La7	La8
x	0.0212(1)	$x_a^{La}+(n-1)/8$, $n=1-8$, $x_a^{La}=0.023(1)$, $z_a^{La}=-0.005(1)$							
z	−0.0032(2)	z_a^{La}	$\frac{1}{2}-z_a^{La}+\Delta z$	$z_a^{La}+\Delta z$	$\frac{1}{2}-z_a^{La}+\Delta z$	z_a^{La}	$\frac{1}{2}-z_a^{La}-\Delta z$	$z_a^{La}-\Delta z$	$\frac{1}{2}-z_a^{La}-\Delta z$
$100U$, B (Å^2)	0.74(1)	0.84(1)							
Mn		Mn3(1)	Mn4(1)	Mn4(2)	Mn4(3)	Mn3(2)			
x		0	1/8	1/4	3/8	1/2			
y		0	0	0	0	0			
z		1/2	Δz_1	$1/2+\Delta z_1$	Δz_1	1/2			
$100U$, B (Å^2)	0.48(2)	0.68(1)							
O1		O1(1)	O1(2)	O1(3)	O1(4)	O1(5)	O1(6)	O1(7)	O1(8)
x	0.4877(4)	$x_a^{O1}+n/8$, $n=1-8$, $x_a^{O1}=0.4869(5)$, $z_a^{O1}=0.0656(5)$							
z	0.0629(3)	$z_a^{O1}+\Delta z_1$	$\frac{1}{2}-z_a^{O1}+\Delta z_1$	$z_a^{O1}+\Delta z_1$	$\frac{1}{2}-z_a^{O1}$	$z_a^{O1}-\Delta z_1$	$\frac{1}{2}-z_a^{O1}-\Delta z_1$	$z_a^{O1}-\Delta z_1$	$\frac{1}{2}-z_a^{O1}$
$100U$, B (Å^2)	1.5(1)	0.42(6)							
O2		O2(1)	O2(2)	O2(3)	O2(4)	O2(5)	O2(6)	O2(7)	O2(8)
x	0.2758(7)	$x_a^{O2}+(n-1)/8$, $n=1-8$, $x_a^{O2}=0.2758(6)$, $y_a^{O2}=0.0325(1)$, $z_a^{O2}=0.7258(9)$							
y	0.0315(1)	y_a^{O2}							
z	0.7251(8)	$z_a^{O2}+\Delta z_1$	$\frac{1}{2}-z_a^{O2}+\Delta z_1$	$z_a^{O2}+\Delta z_1$	$\frac{1}{2}-z_a^{O2}+\Delta z_1$	$z_a^{O2}-\Delta z_1$	$\frac{1}{2}-z_a^{O2}-\Delta z_1$	$z_a^{O2}-\Delta z_1$	$\frac{1}{2}-z_a^{O2}-\Delta z_1$
$100U$, B (Å^2)	0.85(2)	0.67(2)							
S_{400}	0.25(1)	0.0007(1)							
S_{040}	0.05(1)	0.0324(7)							
S_{004}	0.27(1)	0.287(7)							
S_{220}	0.01(1)	0.010(5)							
S_{202}	2.08(2)	0.092(1)							
S_{022}	0.02(1)	0.34(1)							
		Mn1	Mn2	Mn3	Mn4	Mn5			
Mn-O1×2 (Å)	1.9177(3)	1.901(1)	1.901(1)	1.901(1)	1.901(1)	1.901(1)			
Mn-O2×2 (Å)	1.9150(1)	1.945(2)	1.918(2)	1.918(2)	1.918(1)	1.870(1)			
Mn-O2×2 (Å)	1.9214(2)	1.992(2)	1.929(2)	1.929(2)	1.929(1)	1.993(2)			
R_{WP}^{SXRPD} (%)	7.5	6.1							
R_{exp}^{SXRPD} (%)	4.0	1.1							
R_{WP}^{NPD} (%)	5.2								
R_{exp}^{NPD} (%)	4.4								

model accounts for all the resolved satellite Bragg peaks and the Rietveld refinement converges to a lower value for R_B ($R_B=4.0\%$ vs $R_B=4.5\%$). The shifts of the Mn^{4+} octahedra and the La^{3+} ions away from their positions in the average structure refine to $\Delta z_1=-0.018(1)$ and $\Delta z=-0.015(1)$, respectively, at $T=5$ K. We note that as we are dealing with very weak superlattice peaks, we do not expect a substantial improvement in the R_B factor. The region of the SXRPD

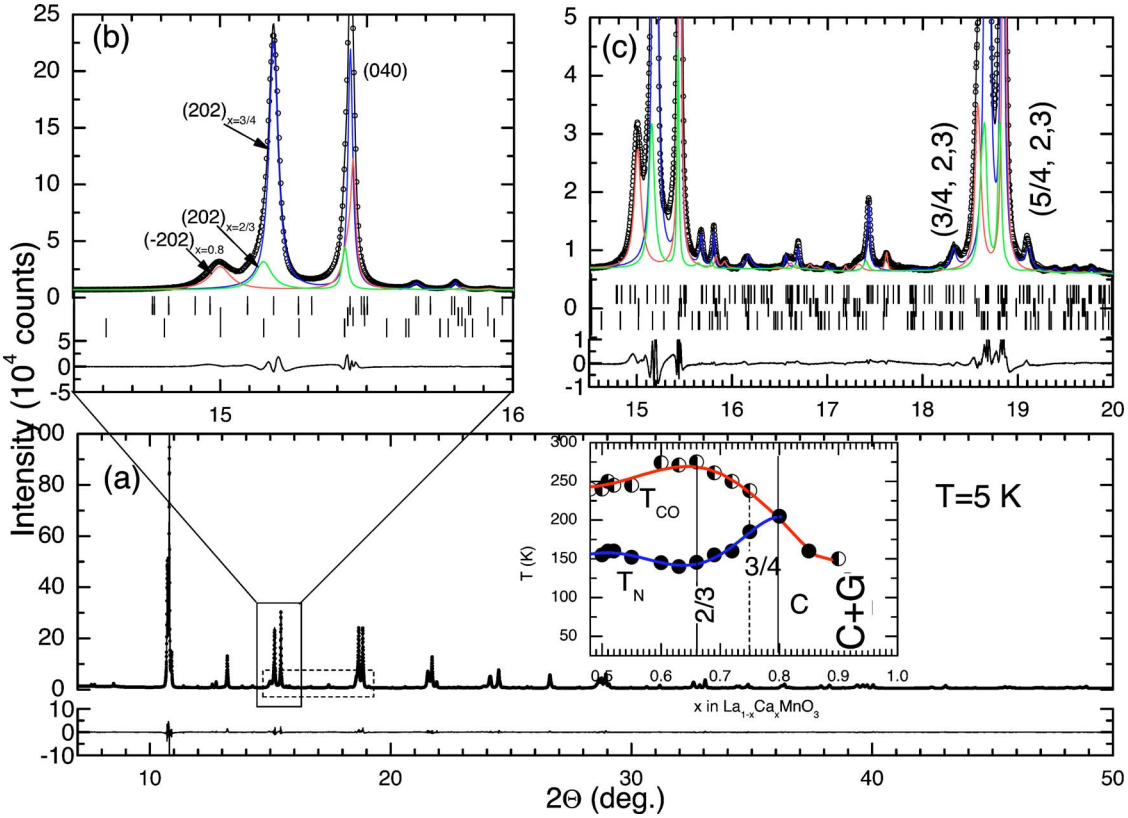

FIG. 2. (Color online.) (a) Observed (○) and calculated (solid line) synchrotron x-ray powder ($T=5$ K, $\lambda=0.50187$ Å) diffraction profiles of $La_{0.25}Ca_{0.75}MnO_3$. Panel (b) shows an expanded region of the Rietveld refinement in the vicinity of the (202)/(040) doublet, where the three-phase coexistence can be clearly seen. (c) An expanded region of the SXRPD profile in which two of the strongest $4a$ superlattice Bragg peaks $\left[\left(\frac{3}{4},2,3\right),\left(\frac{5}{4},2,3\right)\right)$ are present. The lower solid lines show the difference profiles and the tick marks show the reflection positions of the three phases. The inset in panel (a) shows the phase diagram of the $La_{1-x}Ca_xMnO_3$ series for $x>0.5$ from Ref. 5.

profile, in which the most intense satellite Bragg peaks are observed, is shown in panel (c) of Fig. 2.

The refined superstructure model leads to a structure in which the unshifted Mn octahedra at $x=0$ and 0.5 display characteristics that resemble those expected for Jahn-Teller distorted $Mn^{3+}O_6$-units, with two long in-plane Mn-O2 bonds (~2.0 Å), two short in-plane bonds [1.870(1) Å, 1.945(2) Å], and two out-of-plane bonds with intermediate lengths [1.901(1) Å]. The Mn-O bond lengths for the other octahedra remain as in the average structure.

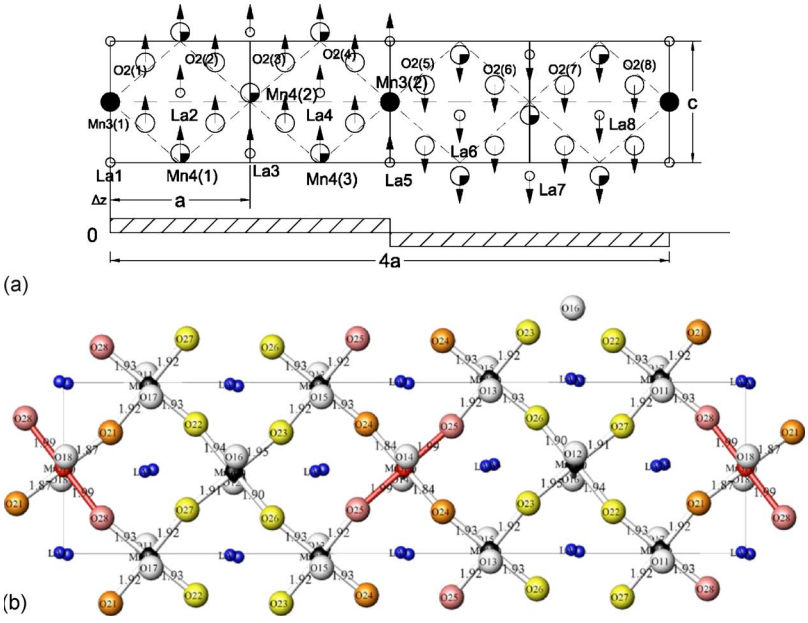

FIG. 3. (a) Schematic drawing of the transverse square modulation model of the $4a$ superstructure on the a-c plane. The Mn and La atoms at $x=0$ and $x=\frac{1}{2}$ remain unshifted, while the other atoms move as the arrows show. (b) (Color online.) Projection into the a-c plane of the superstructure in $La_{0.25}Ca_{0.75}MnO_3$.

Figure 3(b) depicts a projection of the $4a$ superstructure model into the a-c plane. We note that the long in-plane Mn-O bonds form a zigzag pattern, comparable to that observed in the $2a$ superstructure at the $x=0.5$ doping level.[2] As the long Mn-O bond is believed to be related to a $|3z^2-r\rangle$ e_g type orbital, its observed arrangement may be the structural signature of e_g type orbital ordering. Therefore, in analogy with the $2a$ and $3a$ structures, our $4a$ structural model for the $x=\frac{3}{4}$ compound displays a real-space charge and orbital ordering on Mn ions. Of course, based on the Mn-O bond lengths alone, we cannot draw any definitive conclusions about integer charges associated with the "Mn^{3+}" and "Mn^{4+}" sites, as these differ significantly from those encountered in $LaMn^{3+}O_3$ and $CaMn^{4+}O_3$. This intermediate situation, concerning the distribution of the e_g electrons may be related to the presence of small amplitude charge density waves suggested recently.[21–24]

We have also tested alternative structural models such as the paired stripes one,[4] in which Mn^{3+} ions are concentrated in 8.3-Å-wide bistripes with composition $(La,Ca)_3Mn_2^{3+}Mn^{4+}O_9$ and the same orbital order arrangement as in $x=1/2$ compound. The remaining part of the structure consists of Mn^{3+}-depleted regions with composition $5(La,Ca)Mn^{4+}O_3$. Rietveld refinements based on this model were very unstable, presumably because of the presence of three phases and the very large number of free parameters. Nonetheless the Wigner crystal model presented above remains superior, as the paired stripes model predicts a number of second order satellite reflections which are not observed in the present SXRPD data.

B. Temperature variation of the structural and magnetic properties

Figure 4(a) shows the temperature variation of the unit cell parameters for the three phases $4a$, C, and $3a$, as they were estimated by the Rietveld refinements of the SXRPD data at several temperatures. The inset of Fig. 4(a) shows the temperature variation of the monoclinic angle β of the C phase. At 295 K, only a single phase is present adopting the O^* structure $(c>a>b/\sqrt{2})$. On cooling, the b-axis length decreases, while a and c increase slightly. By further cooling, an abrupt change of the unit cell parameters occurs at the temperature interval 180 K$<T<$250 K, with an inflection point, for instance in the $b(T)$ curve, at $T_{CO}\sim 220$ K. In the same temperature regime, the SXRPD patterns develop complicated diffraction peaks, which at lower temperatures can be analyzed successfully with the three-phase structural model mentioned above.

Figure 4(b) shows the temperature variation of the weight fractions of the $4a$, C, and $3a$ phases, while panel (c) of Fig. 4 shows the temperature dependence of the mass magnetic moment, σ (left axis) and its first derivative, $d\sigma/dT$ (right axis), measured in zero field (ZFC) and field cooling (FC) modes in a magnetic field of 100 Oe. The magnetization increases with decreasing temperature below 300 K, displaying a maximum at 247 K, and then decreases rapidly due to the development of the charge-ordered state. The peak in the magnetization curve is not related with a magnetic transition,

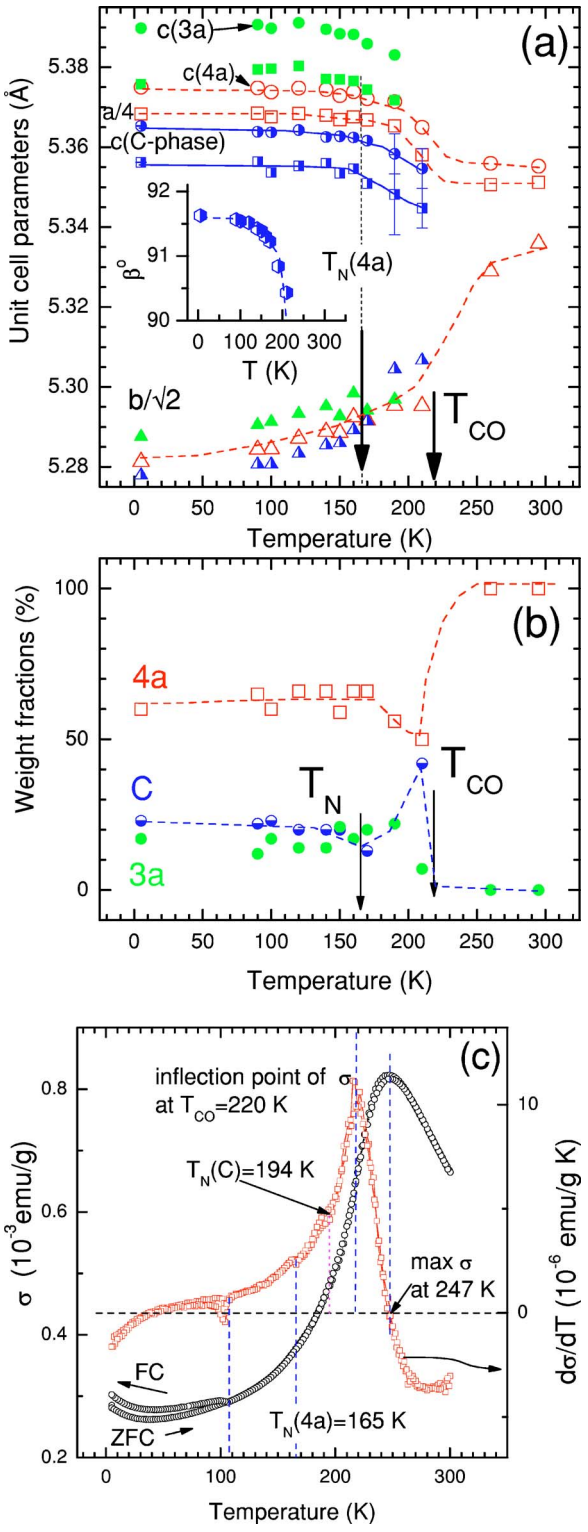

FIG. 4. (Color online.) (a) Temperature variation of the unit cell parameters of the $4a$, C, and $3a$ phases in $La_{0.25}Ca_{0.75}MnO_3$. The inset shows the temperature dependence of the monoclinic angle of the C phase. Circles, squares and triangles correspond to the c, a, and $b/\sqrt{2}$ unit cell axes, respectively. The semifilled, empty and solid symbols correspond to the C, $4a$, and $3a$ phases, respectively. (b) Temperature variation of the weight fractions of the three phases. (c) Temperature variation of the mass magnetic moment, σ and its temperature derivative $d\sigma/dT$.

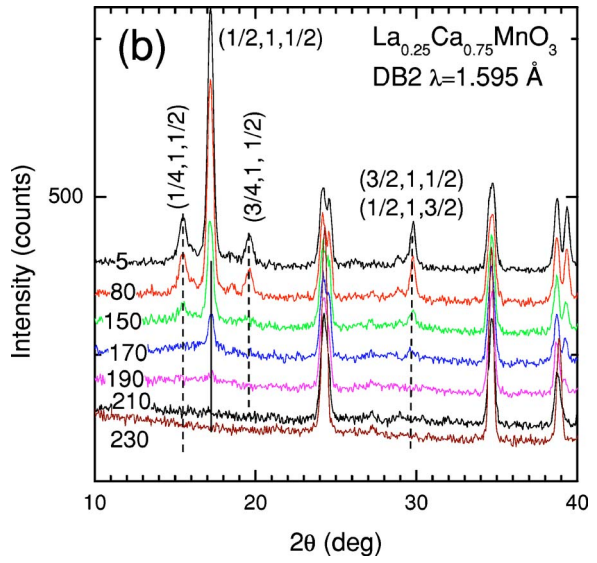

FIG. 5. (Color online.) Selected region of the low-angle neutron-powder-diffraction profile ($\lambda=1.595$ Å) of $La_{0.25}Ca_{0.75}MnO_3$ at several temperatures between 5 and 230 K showing the evolution of the most intense magnetic Bragg peaks (denoted by dashed lines) with temperature.

as the neutron-diffraction data do not show magnetic peaks in this temperature range (see below, Fig. 5). However, this change may be related to the change from uncorrelated (or weakly ferromagnetically correlated) Mn spins to antiferromagnetically correlated ones due to the charge and orbital ordering for $T<T_{CO}$. At 108 K, the magnetization displays irreversible behavior (the ZFC branch does not coincide with the FC one). The SXRPD and NPD data do not show any obvious anomaly corresponding to the onset of the magnetic irreversibility at 108 K. This feature may be related to the dynamic effects between charge-ordered and charge-disordered domains observed recently for the composition $La_{0.23}Ca_{0.77}MnO_3$.[25] The transition to a long-range ordered antiferromagnetic state occurs in the temperature interval $150\ \text{K}<T<195\ \text{K}$, where diffraction peaks of magnetic origin appear in the NPD profiles (see below, Fig. 5). The signature of this transition in the magnetization data can be found in the temperature evolution of the $d\sigma/dT$ curve. Indeed, one can see two characteristic points at 165 and 194 K [Fig. 4(c)], which correspond to the two small shoulders in the $\sigma(T)$ curve. The anomaly at 194 K occurs at the same temperature that the monoclinic angle of the C structure becomes 90°, thereby implying that it is the signature of the antiferromagnetic transition in the C phase. The second point at 165 K coincides with the Néel temperature of the $4a$ phase. These two points will be further discussed in the following section on magnetic neutron scattering. Finally, the inflection point of the $\sigma(T)$ vs T curve, identified at ~220 K is related to the inflection point which appears in the temperature variation of the unit cell parameters of the $4a$ phase. It is at this temperature that the satellite peaks start to develop. Therefore, this temperature represents the charge ordering temperature ($T_{CO}=220$ K). The identification of T_N at 160 K and of T_{CO} at 220 K for the $4a$ phase agrees very well with the results of the specific heat and magnetization measurements of Zheng *et al.*[18]

C. Magnetic structure

Figure 5 shows the temperature evolution of the neutron-powder-diffraction patterns ($\lambda=1.595$ Å) in the angular region where the most intense magnetic Bragg peaks appear. The diffraction peaks in the range $12°\leqslant 2\theta\leqslant 22°$ originate from long-range magnetic order of the Mn spins, as they disappear between $170<T<195$ K. The most intense reflection near $2\theta=17.6°$ belongs to the family of magnetic diffraction peaks, which correspond to the propagation vector $\mathbf{k}_C=[\frac{1}{2},0,\frac{1}{2}]$. Contributions to the intensity of this peak come from the magnetic structures of both the $4a$ and C phases. Below and above this reflection, there are two additional magnetic reflections, whose indexing is consistent with the propagation vector $\mathbf{k}_{1/4}=[\frac{1}{4},0,\frac{1}{2}]$, inherent in the $4a$ superstructure. Remarkably, the intensity of the $(\frac{1}{2},1,\frac{1}{2})$ reflection approaches zero at a different temperature (slightly above 190 K) from that at which the $(\frac{1}{4},1,\frac{1}{2})$ and $(\frac{3}{4},1,\frac{1}{2})$ magnetic reflections disappear (near 170 K). Combining these experimental observations with the results of the magnetization measurements, we conclude that the feature in $\sigma(T)$ at 165 K, corresponds to the onset of antiferromagnetic ordering in the $4a$ phase $[T_N(4a)=165\ \text{K}]$ and the one at 194 K corresponds to the antiferromagnetic ordering transition of the C phase $[T_N(C)=194\ \text{K}]$.

Figure 6 shows the results of the Rietveld refinement of the powder-neutron-diffraction data ($\lambda=2.44$ Å) at 5 K. The intensity of the observed magnetic peaks can be coreectly accounted for when we use a magnetic moment $\mathbf{m}_C=(1.8,0,-1.8)\mu_B$ $(\mathbf{m}\perp\mathbf{k}_C)$ for the impurity C structure, in agreement with Ref. 12, and a magnetic moment $\mathbf{m}_C^{4a}=[1.8(1),0,-1.8(1)]\mu_B$ $(\mathbf{m}\perp\mathbf{k}_C)$ for the $4a$ structure. At this point, we note that the magnetic structure of the $4a$ phase is essentially similar to that of the C-type antiferromagnetic arrangement, contributing significantly to the intensity of the $[\frac{1}{2},1,\frac{1}{2}]$ magnetic Bragg peak. However, the presence of the $[\frac{1}{4},1,\frac{1}{2}]$ and $[\frac{3}{2},1,\frac{1}{2}]$ satellites implies a concomitant magnetic modulation which is related to the structural modulation. In order to account for the magnetic diffraction peaks, we used a $4a\times b\times 2c$ magnetic cell for the $4a$ structure. Keeping in mind that the majority of the magnetic intensity contributions originates from the C-type arrangement of the Mn spins, we can reproduce the magnetic Bragg peaks by assuming a C-type magnetic structure in which the spins of the Mn3(1) and Mn3(2) sites are perturbed in such a way as to account for the presence of the magnetic Bragg peaks which correspond to the $\mathbf{k}_{1/4}$ propagation vector. More specifically, we retained the z-spin component of the Mn(1) and Mn(5) sites identical to that of the C structure, while the corresponding x-spin component was compatible with the $\mathbf{k}_{1/4}$ propagation vector. The best agreement was achieved when the magnetic moment of the Mn4(1), Mn4(2), and Mn4(3) sites was $[\pm 1.8(1),0,\pm 1.8(1)]\mu_B$ and that of the Mn3(1) and Mn3(2) sites $(\pm 3,0,\pm 2)\mu_B$. A projection of the magnetic structure in the $y=0$ plane is shown in the inset of

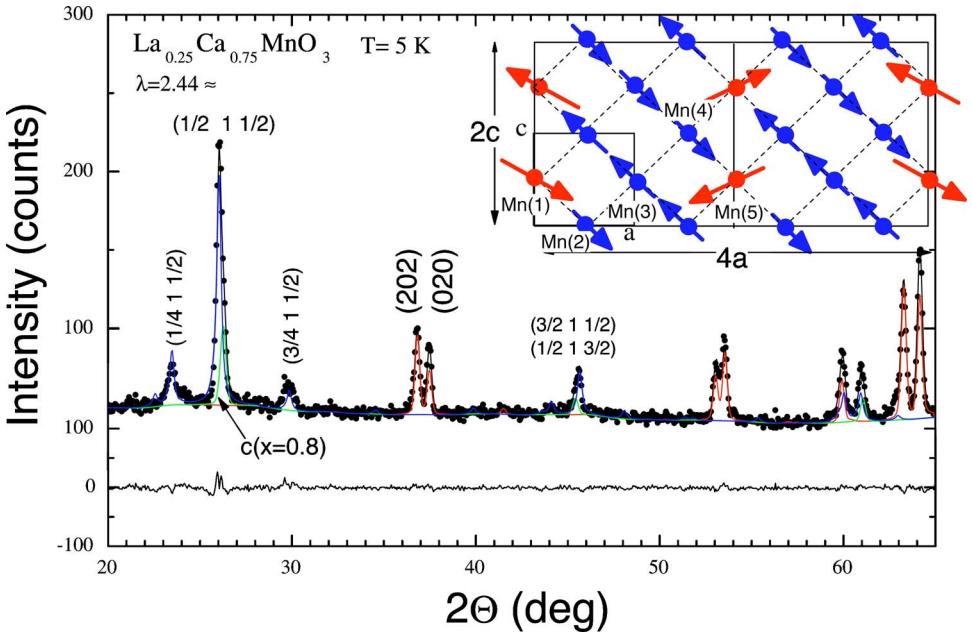

FIG. 6. (Color online.) Rietveld refinement of the low-angle part of the PND profile ($2\theta=20°-70°$, $\lambda=2.44$ Å) of $La_{0.25}Ca_{0.75}MnO_3$ at 5 K. The inset shows a schematic representation of the magnetic structure of the $4a$ phase projected into the a-c plane.

Fig. 6 where it is evident that all the spins in the $y=\frac{1}{2}$ plane are antiferromagnetically coupled with those in $y=0$. Interestingly, this model contains all the essential features of the crystallographic superstructure, explaining magnetically the ordering of the Mn sites. The two Mn sites attributed before to Mn^{3+}-like ions carry a magnetic moment which is canted with respect to the C-type background of the remaining Mn sites. It should be noted that based on the R_B factor, this magnetic model is not unique; however, it captures the main characteristics of the $4a$ superstructure.

IV. DISCUSSION

The majority of phase transformations that occur in the solid state take place by thermally activated atomic movements. There are also transformations that are diffusionless, i.e., from start to completion of the transformation, individual atomic movements are less than one interatomic spacing. Phase separation can originate from kinetic reasons (interplay between driving force and energy barrier), whereupon the system cannot attain equilibrium and is trapped in a metastable state. Furthermore inhomogeneities and disorder can locally favor one phase over another and pin the domain pattern.

Let us discuss the dissociation reaction, which takes place at T_{CO} in the $La_{0.25}Ca_{0.75}MnO_3$ system. By assuming a chemically homogeneous material, the observed phase coexistence might be inherent in the particular physics of manganite perovskites and might be tuned by parameters such as magnetic field and strain. At $T=300$ K, we observe a single phase pattern. Upon cooling to $T_{CO}\approx 220$ K, phase dissociation takes place. We stress that we find this dissociation occurring in several $La_{1-x}Ca_xMnO_3$ samples with calcium content near $x=\frac{3}{4}$ and it is not a peculiarity of the particular sample studied here. This finding may be related to the high-resolution lattice images observed by Mori *et al.*[4] in a sample with the same nominal stoichiometry where they occasionally observed defect structures with $3a$ and $5a$ periodicities. If for the moment we ignore the existence of the $4a$ superstructure, the situation is reminiscent of the dissociation reaction, which produces the $3a$ and C structures, as depicted in the phase diagram in the inset of Fig. 2. It is now important to consider the mechanisms which may explain the complicated phase coexistence on cooling. Atomic diffusion across a few thousands of Å at 220 K is improbable. Therefore, if the low-temperature coexistence was related to preexisting heterogeneity of the A-site cations, reflecting inadequate sample preparation protocol, all phases should be also present at 300 K. However, only one average structure is unambiguously evident from the high-resolution SXRPD profiles. This may imply that the difference in the cell constants of the three phases is so small that leads to diffraction patterns with unresolved overlapping diffraction peaks even at the very high resolution of the present experiments. The small difference of the diffraction peak centroids may then account for the observed selective peak broadening. On the other hand, if the A-site cations are randomly distributed, then a single phase should be present at 300 K. In this case, when the structural transition takes place, large strain may develop between the nucleation centers and the pristine material. Then such strain could prohibit transformation of the complete sample volume in an analogous fashion to the mechanism of martensitic phase transitions where metastable unchanged small domains coexist with the stable transformed phase.

Another remarkable characteristic of the diffraction patterns is the strong temperature dependence of the anisotropic broadening parameters. As we mentioned in the previous section, we successfully took into account the anisotropic Bragg peak broadening using the Stephens formalism.[14,17] At 295 K, the largest strain parameter is $S_{202}(295\ \mathrm{K})=2.0(1)$. On cooling, S_{202} for the $4a$ phase approaches a maximum value at T_{CO} $[S_{202}(T_{CO})\approx 8.1(2)]$ and then decreases smoothly until it reaches a nearly temperature-independent value of $\approx 1.5(1)$. In contrast, when the C phase appears at

$T=210$ K, its S_{202} parameter is significantly larger $[S_{202}(210\ \mathrm{K}) \approx 17.1(3)]$ than that of the $4a$ phase. This value decreases on cooling down to 140 K and then increases slightly approaching a value of 8.2(2) at 5 K.

Here it is interesting to compare our results with those obtained for $Bi_{0.15}Ca_{0.85}MnO_3$ by Llobet *et al.*[26] For this composition, it was proposed that the sample is a heterogeneous two-phase mixture at all temperatures. Despite the single-phase diffraction patterns apparent at 300 K, the very close similarity of the structures of the two components makes it impossible to identify them. However, the structural transition driven by the orbital ordering unmasks the two phases and the macroscopic preexisting phase segregation comes into sight. The two coexisting orthorhombic phases were identified as a minority one—which does not undergo any structural transition on cooling—and a majority one which transforms to monoclinic symmetry at $T=120$ K. Although at first sight, similar behavior appears to be exhibited by the present sample, there are several distinct differences. If $La_{0.25}Ca_{0.75}MnO_3$ was described at 300 K as a three-phase mixture, then the difference in the unit cell parameters and the available resolution would have allowed the identification of at least two ($4a$ and C) of the three phases. As their unit cell parameters differ by ~ 0.03 Å, unambiguous identification of the two phases should have been possible by SXRPD. The most important argument presented by Llobet *et al.*[26] in support of preexisting heterogeneity in $Bi_{0.15}Ca_{0.85}MnO_3$ was that if the strain between the domains would have been the key parameter, then the microstrain terms in the high-temperature orthorhombic phase should have been smaller than those of the strained low-temperature minority orthorhombic phase. However, as the low-temperature majority monoclinic phase exhibited larger microstrain parameters than the minority orthorhombic phase, Llobet *et al.*[26] concluded that macroscopic phase segregation preexisted. In the $La_{0.25}Ca_{0.75}MnO_3$ system, different behavior is observed. The low-temperature minority phase displays significantly larger microstrain parameters than the high-temperature one. In addition, the low-temperature majority phase displays lower values of the microstrain parameters. These observations imply that a different mechanism is responsible in the present system. In $Bi_{0.15}Ca_{0.85}MnO_3$, the chemical heterogeneity was attributed to deficiency of the (Bi, Ca) sites. The volatility of Bi during the solid state preparation is well known. If the same type of deficiency is present in the (La, Ca) sites of $La_{0.25}Ca_{0.75}MnO_3$, then similar behavior would have been expected for related samples with $x=\frac{1}{2}$, $\frac{2}{3}$, and $\frac{4}{5}$, where similar preparation conditions are used. Therefore it seems reasonable to conclude that in the case of the $La_{1-x}Ca_xMnO_3$ series with $0.5<x<0.9$ the samples are stoichiometric at ambient temperature thereby ruling out the cation non-stoichiometry scenario.

The other classical model for explaining phase coexistence is that of a martensitic transformation. It has been indeed proposed that the charge ordering (CO) transition in some of the manganite perovskites exhibits clear signatures of a matrensitic transformation. For example, micrographs of the $Bi_{0.2}Ca_{0.8}MnO_3$ system below T_{CO} show lenticular charge ordered domains.[27] Martensitic transformations proceed by diffusionless formation of martensitic islands within a parent phase crystal lattice. Since the crystal lattices of the two phases involved are different, in order for them to fit together, significant atomic displacements producing elastic strain are required (accommodation strain). As the temperature is reduced, the accommodation strain grows and thermoelastic equilibrium is established defining the amount of martensite and the remaining high-temperature phase. Let us examine if our results can be explained in terms of a martensitic transformation scenario. The minority phases display large anisotropic strain with S_{202} being always the dominant microstrain parameter. We also stress that the values of the microstrain parameters increase as the temperature is lowered. This behavior is not compatible with that for a conventional martensitic transformation. If the martensitic transition was the dominant mechanism, then one would expect the majority phase to exhibit large microstrain contrary to the experimental results.

The large microstrain of the minority phases could result if these were of submicron size and were occurring in parts of the crystallites that for some reason were prevented from transforming into the $4a$ structure. The accommodation of the $3a$ and C structures inside the $4a$ structure produces large fluctuation of the strain field in the $[h0h]$ direction. Alternatively, since we are near the C-structure phase boundary, short-range concentration inhomogeneities (small regions with large fluctuation of the dopant level x) could produce this coexistence. The $4a$ structure due to the small difference from the C structure demands a high uniformity in the La/Ca ratio in order to form. Based on the simple superstructure models developed above, the majority of the superstructure unit cell contains parts which adopt the C structure. Consequently, small perturbations of the La/Ca ratio could prevent formation of the $4a$ phase. This type of coexistence is inherent in the charge ordering phenomena as the real space charge localization period increases, for instance, from $2a$ to $3a$ and eventually to $4a$ in the present system. In order for charge ordering to take place, a threshold value of crystallite size is necessary. In small crystallites, the surface energy may be comparable to the charge ordering energy, thereby prohibiting the CO transformation. We must note, however, that the microstructural parameters both above and below the CO temperature do not show small diffraction domains but rather that their energy is governed by microstrain effects. We also note the arguments of Ahn *et al.*[28] who have proposed that "texturing" effects, similar to ours, may be due to the intrinsic complexity of the system with strong coupling between the electronic and elastic degrees of freedom leading to local energetically favorable configurations and providing a natural mechanism for the self-organized inhomogeneities over micrometer scales.

Finally we refer to the very good agreement of our results with those of Tao *et al.*[25] for a sample with stoichiometry $La_{0.23}Ca_{0.77}MnO_3$. High-resolution dark field images of fundamental reflections and the corresponding CO superlattice spots revealed the coexistence of the charge ordered $4a$ phase and the charge-disordered C phase. In agreement with our results, the observed coexistence cannot be attributed to either chemical segregation or composition variations in the sample but most probably it is related to strong magnetoelastic effects.

V. CONCLUSION

In conclusion, we have experimentally demonstrated that the $La_{1/4}Ca_{3/4}MnO_3$ system exhibits a complicated transition at T_{CO}. For $T<T_{CO}$, the high-temperature phase transforms to a three-phase mixture comprising the $4a$-[60(1)%], C-[23(1)%], and $3a$-[17(2)%] structures. The $4a$ superstructure results from a transverse modulation (perpendicular to **k**) of the positional atomic parameters with polarization along the c axis. The observed phase coexistence is characteristic of the very complex crystal chemistry of the manganite perovskites.

ACKNOWLEDGMENTS

We thank the ESRF and the ILL for provision of beamtime and Dr. A. N. Fitch for useful discussions and help with the synchrotron x-ray diffraction experiments.

[1] J. B. Goodenough, *Magnetism and Chemical Bond* (Interscience, New York, 1963); *Colossal Magnetoresistive Oxides*, edited by Y. Tokura (Gordon and Breach, New York, 2000); *Colossal Magnetoresistance, Charge Ordering and Related Properties of Manganese Oxides*, edited by C. N. R. Rao and B. Raveau (World Scientific, Singapore, 1998); *Physics of Manganites*, edited by T. A. Kaplan and S. D. Mahanti (Kluwer, Dordrecht, 1999); C. N. R. Rao, A. Arulraj, A. K. Cheetham, and B. Raveau, J. Phys.: Condens. Matter **12**, R83 (2000); A. P. Ramirez, *ibid.* **9**, 8171 (1997); Y. Tokura and Y. Tomioka, J. Magn. Magn. Mater. **200**, 1 (1999); J. M. D. Coey, M. Viret, and S. von Molnar, Adv. Phys. **48**, 167 (1999); M. B. Salamon and M. Jaime, Rev. Mod. Phys. **73**, 583 (2001); E. Dagotto, T. Hotta, and A. Morea, Phys. Rep. **344**, 1 (2001); E. L. Nagaev, *ibid.* **346**, 387 (2001); A. J. Millis, Nature (London) **392**, 147 (1998).

[2] P. G. Radaelli, D. E. Cox, M. Marezio, and S.-W. Cheong, Phys. Rev. B **55**, 3015 (1997).

[3] P. G. Radaelli, D. E. Cox, L. Capogna, S.-W. Cheong, and M. Marezio, Phys. Rev. B **59**, 14 440 (1999).

[4] S. Mori, C. H. Chen, and S.-W. Cheong, Nature (London) **392**, 473 (1998).

[5] M. Pissas and G. Kallias, Phys. Rev. B **68**, 134414 (2003).

[6] G. Kallias, M. Pissas, E. Devlin, and A. Simopoulos, Phys. Rev. B **65**, 144426 (2002).

[7] J. C. Loudon, S. Cox, A. J. Williams, J. P. Attfield, P. B. Littlewood, P. A. Midgley, and N. D. Mathur, Phys. Rev. Lett. **94**, 097202 (2005); N. Mathur and P. Littlewood, Phys. Today **56**, 25 (2003); J. C. Loudon, N. D. Mathur, and P. A. Midgley, Nature (London) **420**, 797 (2002).

[8] A. Daoud-Aladine, J. Rodríguez-Carvajal, L. Pinsard-Gaudart, M. T. Fernández-Díaz, and A. Revcolevschi, Phys. Rev. Lett. **89**, 097205 (2002).

[9] K. J. Thomas, J. P. Hill, S. Grenier, Y-J. Kim, P. Abbamonte, L. Venema, A. Rusydi, Y. Tomioka, Y. Tokura, D. F. McMorrow, and M. van Veenendaal, Phys. Rev. Lett. **92**, 237204 (2004).

[10] J. Herrero-Martín, J. García, G. Subías, J. Blasco, and M. Concepción Sánchez, Phys. Rev. B **70**, 024408 (2004).

[11] E. E. Rodriguez, Th. Proffen, A. Llobet, J. J. Rhyne, and J. F. Mitchell, Phys. Rev. B **71**, 104430 (2005).

[12] M. Pissas, G. Kallias, M. Hofmann, and D. M. Többens, Phys. Rev. B **65**, 064413 (2002).

[13] C. H. Chen and S.-W. Cheong, Phys. Rev. Lett. **76**, 4042 (1996).

[14] J. Rodriguez-Carvajal, Physica B **192**, 55 (1993).

[15] A. C. Larson and R. B. von Dreele, *General Structure Analysis System (GSAS)*, Los Alamos National Laboratory, 2000; B. H. Toby, J. Appl. Crystallogr. **34**, 210 (2001).

[16] L. W. Finger, D. E. Cox, and A. P. Jephcoat, J. Appl. Crystallogr. **27**, 892 (1994).

[17] P. W. Stephens, J. Appl. Crystallogr. **32**, 281 (1999).

[18] R. K. Zheng, A. N. Tang, Y. Tang, W. Wang, G. Li, X. G. Li, and H. C. Ku, J. Appl. Phys. **94**, 514 (2003).

[19] H. Böhm, Acta Crystallogr., Sect. A: Cryst. Phys., Diffr., Theor. Gen. Crystallogr. **31**, 622 (1975).

[20] H. Böhm, Z. Kristallogr. **143**, 56 (1976).

[21] L. Brey, Phys. Rev. Lett. **92**, 127202 (2004).

[22] G. Varelogiannis, Phys. Rev. Lett. **85**, 4172 (2000).

[23] V. Ferrari, M. Towler, and P. B. Littlewood, Phys. Rev. Lett. **91**, 227202 (2003).

[24] G. C. Milward, M. J. Calderón, and P. B. Littlewood, Nature (London) **433**, 607 (2005).

[25] J. Tao, D. Niebieskikwiat, M. B. Salamon, and J. M. Zuo, Phys. Rev. Lett. **94**, 147206 (2005).

[26] A. Llobet, C. Frontera, J. L. Garcí-Muñoz, C. Ritter, and M. A. G. Aranda, Chem. Mater. **12**, 3648 (2000).

[27] V. Podzorov, B. G. Kim, V. Kiryukhin, M. E. Gershenson, and S.-W. Cheong, Phys. Rev. B **64**, 140406(R) (2001).

[28] K. H. Ahn, T. Lookman, and A. R. Bishop, Nature (London) **428**, 401 (2004).